

ARTICLE

Received 1 Aug 2014 | Accepted 22 May 2015 | Published 21 Jul 2015

DOI: 10.1038/ncomms8628

OPEN

Towards a mechanistic understanding of carbon stabilization in manganese oxides

Karen Johnson¹, Graham Purvis², Elisa Lopez-Capel³, Caroline Peacock⁴, Neil Gray², Thomas Wagner², Christian März², Leon Bowen⁵, Jesus Ojeda⁶, Nina Finlay¹, Steve Robertson¹, Fred Worrall⁷ & Chris Greenwell⁷

Minerals stabilize organic carbon (OC) in sediments, thereby directly affecting global climate at multiple scales, but how they do it is far from understood. Here we show that manganese oxide (Mn oxide) in a water treatment works filter bed traps dissolved OC as coatings build up in layers around clean sand grains at 3%w/wC. Using spectroscopic and thermogravimetric methods, we identify two main OC fractions. One is thermally refractory (> 550 °C) and the other is thermally more labile (< 550 °C). We postulate that the thermal stability of the trapped OC is due to carboxylate groups within it bonding to Mn oxide surfaces coupled with physical entrapment within the layers. We identify a significant difference in the nature of the surface-bound OC and bulk OC. We speculate that polymerization reactions may be occurring at depth within the layers. We also propose that these processes must be considered in future studies of OC in natural systems.

¹School of Engineering and Computing Sciences, Durham University, South Road, Durham DH1 3LE, UK. ²School of Civil Engineering and Geosciences, Devonshire Walk, Newcastle University, Newcastle upon Tyne NE1 3RE, UK. ³School of Agriculture, Food and Rural Development, Newcastle University, Newcastle upon Tyne NE1 7RU, UK. ⁴Earth Surface Science Institute, School of Earth and Environmental Sciences, University of Leeds, Leeds LS2 9JT, UK. ⁵Department of Physics, Durham University, South Road, Durham DH1 3LE, UK. ⁶Experimental Techniques Centre, Institute of Materials and Manufacturing, Brunel University, Uxbridge UB8 3PH, UK. ⁷Department of Earth Sciences, Durham University, South Road, Durham DH1 3LE, UK. Correspondence and requests for materials should be addressed to K.J. (email: karen.johnson@durham.ac.uk).

Recent estimates suggest that after rocks (70 million Gt of organic carbon), soils (2,500 Gt) and marine sediments (3,000 Gt) account for the largest reservoirs of organic carbon on Earth^{1,2}. It is thought that all of this carbon is intimately mixed with minerals². Many researchers have studied the nature of mineral-stabilized organic carbon in soils³ and marine sediments⁴, but the majority of these studies are the equivalent of 'biogeochemical black boxes' where inputs and outputs can be estimated but the internal mechanisms operating in these natural systems are rarely clear due to their inherent complexity. We therefore need to look at simpler, more controlled systems to extract the fundamental mechanistic of mineral-carbon interactions.

Manganese is known to strongly interact with dissolved organic carbon (DOC)⁵⁻⁷. Its global role in the stabilization of carbon in sediments, however, is almost entirely unconstrained. Roy *et al.*⁸ recently described the close association between both reactive iron (Fe) and reactive manganese (Mn) with organic carbon (OC) in the marine sediments off the Californian and Oregon coast in the United States. They⁸ found that there was a stronger correlation between Fe and OC compared with Mn and OC and postulated that this was because reactive Mn was more mobile during diagenesis. Lalonde *et al.*⁴ more recently confirmed that Fe-associated OC (Fe-OC) accounts for up to 21% of marine sediment OC, emphasizing the importance of mineral-organic interactions as critical components of the global carbon cycle. However, neither of these studies is able to comment in detail on the specific mechanisms behind the OC stabilization by these redox active metal oxides. This is due to the inherent heterogeneity of natural systems, in terms of microbiology, fluctuating environmental conditions and the mixed mineral assemblages they represent.

To further add to the complexity of studying mineral-OC interactions in natural systems, most OC in sediments is molecularly uncharacterized carbon (MUC)⁹.

Traditionally, OC in sediments has been analysed using acids/alkalis or solvents for extraction and then chromatography for characterization, but these methods are flawed due to the changes induced in the organic carbon during extraction¹⁰. Thermal gravimetric analysis has been shown to differentiate between pools of organic carbon, broadly defined as 'thermally labile' (released at temperatures <550 °C) and 'thermally refractory'¹¹⁻¹³ (released at temperatures >550 °C). However, both solvent extraction and thermal analysis can suffer from analytical artefacts requiring other, independent analyses. We use X-Ray photoelectron spectroscopy to study the OC bonding environment without either solvent or thermal extraction. Thermally refractory OC in soils is traditionally thought to be composed of black carbon¹¹, but it is only an end member in a continuum of thermally refractory OC, as humin is also thermally stable¹⁴. Black carbon is formed by the incomplete combustion¹³ of organic carbon. Humin (or 'protokerogen') is thought to be organic carbon that is strongly bound to mineral surfaces¹⁴. Current theories on how OC becomes partitioned into the thermally refractory humin fraction include selective preservation of refractory molecules, physical protection of OC by mineral occlusion (entrapment of OC within the mineral matrix) and geopolymerization¹⁵⁻¹⁷.

Geopolymerization describes the oxidative polymerization of low molecular weight monomers to humic substances that can be catalysed by mineral surfaces¹⁷. Birnessite is one of the most common Mn oxides in terrestrial (for example, in soils¹⁸ and natural aquatic systems¹⁹) and marine environments (for example in oceanic ferromanganese nodules^{20,21} and in pelagic sediments^{21,22}). Birnessite also catalyses the polyphenol-Maillard reaction²³, which generates humic polymers. In contrast, Mn

oxides can break down high molecular weight (HMW) humic substances into lower molecular weight (LMW) organic molecules⁶. Whether Mn oxides humify organic molecules into larger HMW molecules or break them down them into smaller LMW molecules is not fully understood but is likely to depend on the balance between oxidants (including oxygen and Fe/Mn oxides) and reductants (such as DOC) in the system²⁴. Our study addresses a major gap in understanding about the mechanism of how OC and sediments interact at a molecular and individual mineral scale, invoking both of these aforementioned reaction pathways in the same micro-environment.

In contrast to the 'black box' approach of studying natural systems, we decided to present experimental data from a more controlled non-natural system. Our data are from a clean water treatment works (WTW) where the main inputs and outputs of Mn and DOC are well constrained. The WTW filter bed consists of birnessite-coated sands (confirmed with extended X-ray absorption fine structure (EXAFS) spectroscopy, data not shown), which represent a far simpler and relatively homogenous mineralogy compared with natural marine sediments or terrestrial soils. Studying this simplified system has significant advantages over natural samples, as we are able to look at the specific chemical mechanisms involved in OC stabilization in concentrated mineral assemblages, largely without biotic interference (see below). This approach enables us to show that the birnessite, one of the most common forms of Mn oxide in marine²⁰⁻²² and terrestrial environments^{18,19}, builds up in 'onion shell' like layers in WTWs, trapping DOC at 3%w/w C (0.5%w/w inorganic carbon is also present). We call the trapped organic carbon 'manganese associated organic carbon' (Mn-OC). We use a novel combination of micro-Fourier transform infrared spectroscopy (FTIR), fluorescence spectroscopy, thermogravimetric analysis (TGA) and X-ray photoelectron spectroscopy (XPS) to analyse this Mn-OC and identify differences between Mn-OC bound at the surface of the Mn oxide coatings (that is, the outermost layer of Mn oxide) and Mn-OC present in the bulk Mn oxide coatings.

Results

Sampling. The birnessite-coated sand is from a clean water treatment works (WTW) gravity filter bed designed to remove soluble Mn ($\sim 0.2 \text{ mg l}^{-1}$) from the influent water (see Methods for further details). The influent water contains natural DOC $\sim 10 \text{ mg l}^{-1}$ with a $\delta^{13}\text{C}$ signature of $\sim -27\%$ ref. 25 and a small amount of a cationic flocculant (see Methods for further details). The pH is raised to pH 9.2 by flash liming to optimize abiotic manganese removal via precipitation of birnessite as coatings on the sand grains and as Mn oxide particulates in between the grains. Basal respiration is not detectable. It should be noted that not all influent Mn (or DOC) is removed. The filter bed is backwashed on a daily basis to remove particulate Mn oxide to ensure that porosity is retained. The Mn that stays in the filter bed builds up as birnessite coatings ($\sim 100 \mu\text{m}$ thick) on sand grains (see Fig. 1). We refer to 'surface bound Mn-OC' as the organic carbon present on the outermost surface of the intact birnessite coatings, while 'bulk Mn-OC' refers to the organic carbon present throughout the bulk of the birnessite coatings (where bulk material was generated by carefully dislodging the birnessite coatings from the sand grains and sieving to produce the 63-149 μm fraction).

Surface bound Mn-OC via FTIR and fluorescence spectroscopy.

The surface of the intact birnessite coatings was washed repeatedly in de-ionized water (as a control) and in 1 M NaOH (in an attempt to remove surface bound OC) and analysed by micro-FTIR

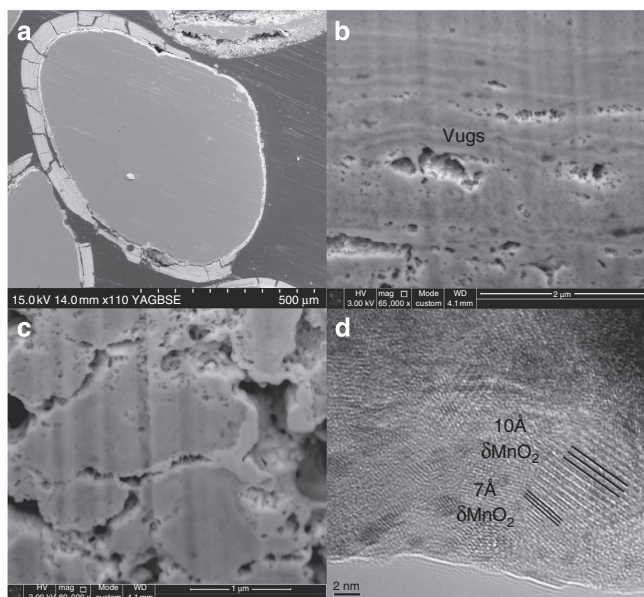


Figure 1 | SEM, TEM and FIB images of birnessite coating. (a) Scanning electron micrograph showing intact birnessite coating on sand grains. (b) Focused ion beam image of birnessite coating showing light and dark laminae at both μm and nm scale. (c) FIB image showing close-up of vugs within birnessite coating, apparently partially infilled with lighter (in colour) precipitates. (d) Transmission electron micrograph of birnessite coating showing both 7 and 10 Å poorly crystalline birnessite (akin to δMnO_2). Images **a–c** are all in back-scattered mode showing atomic contrast.

spectroscopy to observe visible Mn-OC (see Fig. 2 where red colours show high OC concentration and blue colours show low OC concentrations) and fluorescence spectroscopy (Table 1) to identify and characterize surface-bound Mn-OC.

The micro-FTIR images show that OC distribution on the surface of the birnessite coating is not homogenous (Fig. 2 shows three spot analyses representing relatively high, medium and low OC concentration in each case). In the micro-FTIR spectra, the pale blue bands highlight molecules adsorbing between $3,000$ and $2,800\text{ cm}^{-1}$, which can be attributed to C-H groups²⁶. This C-H contribution is less evident for the birnessite that has been washed in NaOH, suggesting that some organics are removed from the birnessite during this wash step. However, the persistence of the broad shoulder between $3,000$ and $2,800\text{ cm}^{-1}$ after washing in NaOH indicates that not all the C-H bonds are removed, confirming a strong association between this remaining OC and the birnessite.

The presence of the band around $1,750\text{ cm}^{-1}$ can be assigned to the stretching $\text{C}=\text{O}$ ($\nu_{\text{C}=\text{O}}$)²⁷ and is usually attributed to the presence of carbonyl moieties (such as those found in carboxylic groups, esters, ketones). The band around $1,400\text{ cm}^{-1}$ (ref. 28) can be assigned to the symmetric stretching of C-O of carboxylate groups ($\nu_{\text{sym COO}^-}$), whereas the shoulder corresponding to the anti-symmetric stretching vibration ($\nu_{\text{asym COO}^-}$) is observed at $1,595\text{ cm}^{-1}$ (ref. 29) in the sample washed in de-ionized water and $1,565\text{ cm}^{-1}$ in the sample washed in NaOH. The absorption band around $1,650\text{ cm}^{-1}$ indicates the presence of carbon double bonded to carbon ($\text{C}=\text{C}$) such as in alkenes or aromatic rings³⁰. Although the peak at $1,750\text{ cm}^{-1}$ (mostly attributable to carboxylic groups) is not readily apparent after washing with NaOH, those at $1,565$ and $1,400\text{ cm}^{-1}$ (attributable to carboxylate groups) and those at $1,650\text{ cm}^{-1}$ (attributable to alkenes/aromatic groups) are all apparent in the most concentrated spot analyses of the birnessite washed in NaOH

(Fig. 2, bottom, spots 1 and 2). These observations suggest that carbonyl moieties present in carboxylate groups, and alkenes/aromatic groups, form part of the more stable carbon pool that is not removed by NaOH.

Extensive studies made on metal complexes of carboxylic acids have established an empirical correlation between the position of the symmetric stretching ($\nu_{\text{sym COO}^-}$) and asymmetric stretching ($\nu_{\text{asym COO}^-}$) of carboxylate groups and the difference in frequency between them ($\Delta\nu$)^{31–35}. In our case, as can be seen in Fig. 2, $\Delta\nu \approx 165\text{--}195\text{ cm}^{-1}$ suggests that the carboxylate groups could be forming either bridging or bidentate complexes with the Mn-OH functional groups on the birnessite surface, in a ligand exchange complexation reaction^{31–34}. Other authors have found that carboxylate can complex amorphous manganese oxides (poorly crystalline hexagonal birnessites) have a $\Delta\nu \approx 220$ (refs 26,36) and also assigned to the formation of either bridging or bidentate carboxylate complexes.

The broad band around $3,200\text{ cm}^{-1}$ present in all the spectra corresponds to the stretching of O-H (ν_{OH}) and can be attributed to the presence of hydroxides, alcohols or, more likely, water. The bands observed around $2,550\text{ cm}^{-1}$ (ref. 37) are most probably caused by linearly adsorbed CO_2 , where the molecules interact via one oxygen atom with metal cations³⁸.

To explore any redox reactions between the sequestered OC and birnessite we performed fluorescence spectroscopy (Table 1) on the original DOC molecules (from the peaty uplands of the WTW catchment) and on the soluble fraction of the surface Mn-OC, which was released into de-ionized water (amended to pH 5 like the original peaty water DOC) after reaction with the birnessite surface, called Mn-OC_{DOC}. Both the original DOC and Mn-OC_{DOC} have a large fraction of fulvic-like material, with peak A³⁹ (fulvic-like fluorophore of intensity 30) twice the intensity of peak C³⁹ (humic-like fluorophore of intensity 16) (see Table 1).

There is a blue shift in the emission wavelength from original peaty water DOC to Mn-OC_{DOC} in both the Peak A (41 nm) and Peak C (40 nm) fluorophores³⁹. This suggests that the reaction of the birnessite with the original DOC results in the release of transformed organic molecules, Mn-OC_{DOC}, which have a lower aromaticity than the original DOC for both Peak A and Peak C³⁹. This was anticipated as Mn oxides are capable of transforming HMW organic molecules into LMW molecules via oxidative transformations, which involves breaking aromatic carbon-carbon bonds⁶.

Taken together, the FTIR spectroscopy and fluorescence spectroscopy data suggest that the DOC is strongly adsorbed to the birnessite via carboxylate functional groups, and that, as a result of the adsorption reaction, the DOC is at least partially transformed into more aliphatic molecules.

Bulk Mn-OC via TGA and XPS analysis. To gain a better understanding on the kinetic properties of the Mn-OC in the birnessite coating we next investigated the thermal reactivity of the carbon using TGA. The partitioning of carbon between organic (OC, 3.0%w/wC) and inorganic (IC, 0.5%w/wC) pools based on the TGA (up to $800\text{ }^\circ\text{C}$) of the bulk material is shown in Fig. 3a as the m/z 44 (CO_2 and N_2O —see Methods section) trace. Carbon dioxide (m/z 44) is detected at $200\text{--}375\text{ }^\circ\text{C}$ (associated with thermally labile OC) and $550\text{--}750\text{ }^\circ\text{C}$ (associated with thermally refractory OC). The thermally labile fraction is represented by the pink peak components (labelled nos. 2–4) and represents $\sim 89\%$ of the Mn-OC, which is available to $800\text{ }^\circ\text{C}$. The thermally refractory fraction is represented by the blue peak component (labelled no. 6) and represents $\sim 11\%$ of the Mn-OC, which is available to $800\text{ }^\circ\text{C}$. Inorganic carbon (IC) as calcite, with no interference by other decomposition reactions, gives a weight

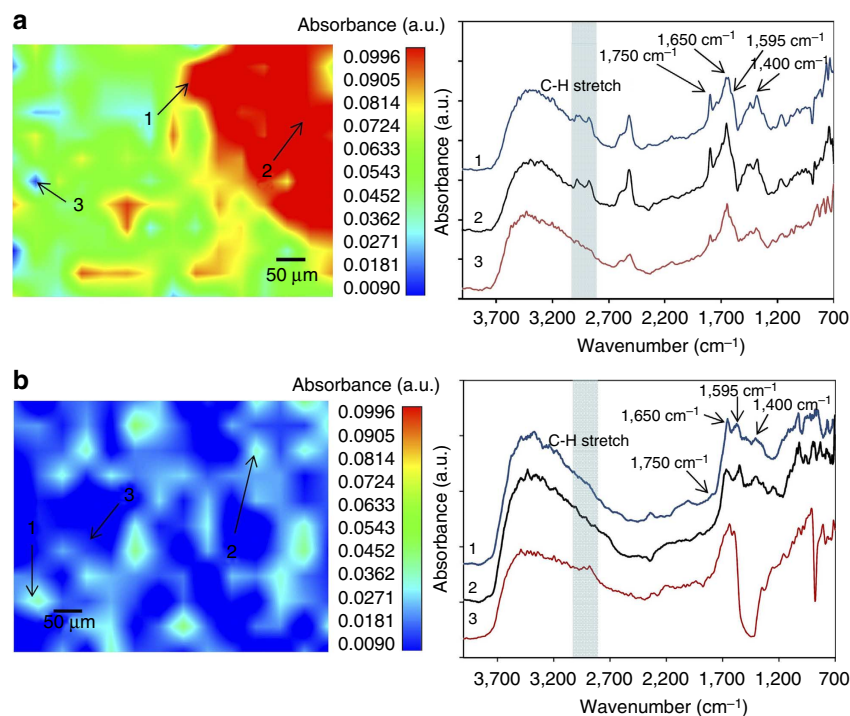


Figure 2 | Micro-FTIR images of birnessite coating. (a) Micro-FTIR spectroscopy image and spectra of the surface of an intact birnessite coating (washed repeatedly in de-ionized water) showing presence of organic carbon (at three separate points representing low, medium and high OC concentrations). (b) Micro-FTIR spectroscopy image and spectra of a (different) surface of an intact birnessite coating (washed repeatedly with 1M NaOH) showing presence of organic carbon (at 3 separate points representing low, medium and high OC concentrations) at lower concentrations than when washed in de-ionized water. Red-yellow colours show higher concentration of OC and green-blue colours show lower concentration of OC. In the spectra, the blue band shows the C-H stretch between 3,000 and 2,800 cm^{-1} and also labelled are the C=C (1,650 cm^{-1}) and carbonyl (1,750 cm^{-1}) peaks as well as the $\nu_{\text{sym}} \text{COO}^-$ (1,400 cm^{-1}) and $\nu_{\text{asym}} \text{COO}^-$ (1,595 cm^{-1} in (a) and 1,565 cm^{-1} in (b)) peaks.

Table 1 | Fluorescence spectroscopy data for DOC and Mn-OC_{DOC}.

All at pH5	Peak A—'fulvic-like'	Peak C—'humic-like'
DOC (from peaty water)	223:454 (30)	342:450 (16)
Mn-OC _{DOC}	213:413 (30)	296:410 (16)

DOC, dissolved organic carbon; Excitation:emission wavelengths (nm, with maximum intensity in adsorption units in brackets) of Peak A (fulvic-like) and Peak C (humic-like) for both the original peaty water DOC and the Mn-OC_{DOC}. $n=3$ and s.d. values <2 nm and <0.5 adsorption units.

loss at around 720 °C. The purple peak (labelled no. 7) present at 712 °C is assigned to IC breakdown. This is corroborated by an endothermic reaction at 712 °C, visible in the differential scanning calorimetry (DSC) curve (see Fig. 3b).

Figure 3b shows that water (m/z 18) is detected at 25–200 °C and 200–400 °C and constitutes the largest proportion of the overall weight loss. Water loss is associated with surface dehydration and mineralogical transformation of birnessite^{40,41} and decomposition of OC^{42,43}. There is limited available data on the TGA of synthetic birnessite^{44,45} but more detailed studies on other Mn oxides including manganite (MnOOH)⁴⁰ and γMnO_2 (ref. 41) show a progressive weight loss from 200 to 580 °C, which is due to water and some oxygen loss, with a sudden and significant weight loss at 620 °C, assigned to a mineralogical transformation to bixybite, Mn_2O_3 (refs 40,41,44). The DSC curve shows exothermic reactions at 270 and 600 °C, which could be associated with the breakdown of labile and refractory OC, respectively. The exothermic reaction at 600 °C is very near the temperature (620 °C) where the mineralogical transformation of Mn oxides to bixybite occurs^{40,41,44}. A change in mineralogy at

620 °C may therefore explain some of the release of the thermally refractory Mn-OC suggesting that physical encapsulation may be a factor in determining how Mn-OC is sequestered and when Mn-OC is released.

Deconvolution (see Methods section) of the TGA data (Fig. 3a) reveals that thermally labile Mn-OC consists of at least three peak components, potentially representing three types of OC, which have previously been assigned as broadly cellulose-like (peak 2), lignin-like (peak 3) and more polycondensed material (peak 4)⁴² with cellulosic-like carbon dominating. The small peak present at 500 °C (peak 5) is typically associated with *in situ* generation of a char, which is an artefact produced as an intermediate product from the thermal decomposition of thermally labile-cellulosic-like material⁴⁶. Leifeld⁴⁶ examined the potential for discriminating between two types of thermally refractory OC: first, one which is inherently present in soils and sediments, and second, one which is likely produced as an artefact of the heating process (char). Leifeld⁴⁶ concluded that exotherms derived at 520 °C or higher are derived exclusively from thermally refractory OC that is inherently present in the sample and not from artefact chars. We

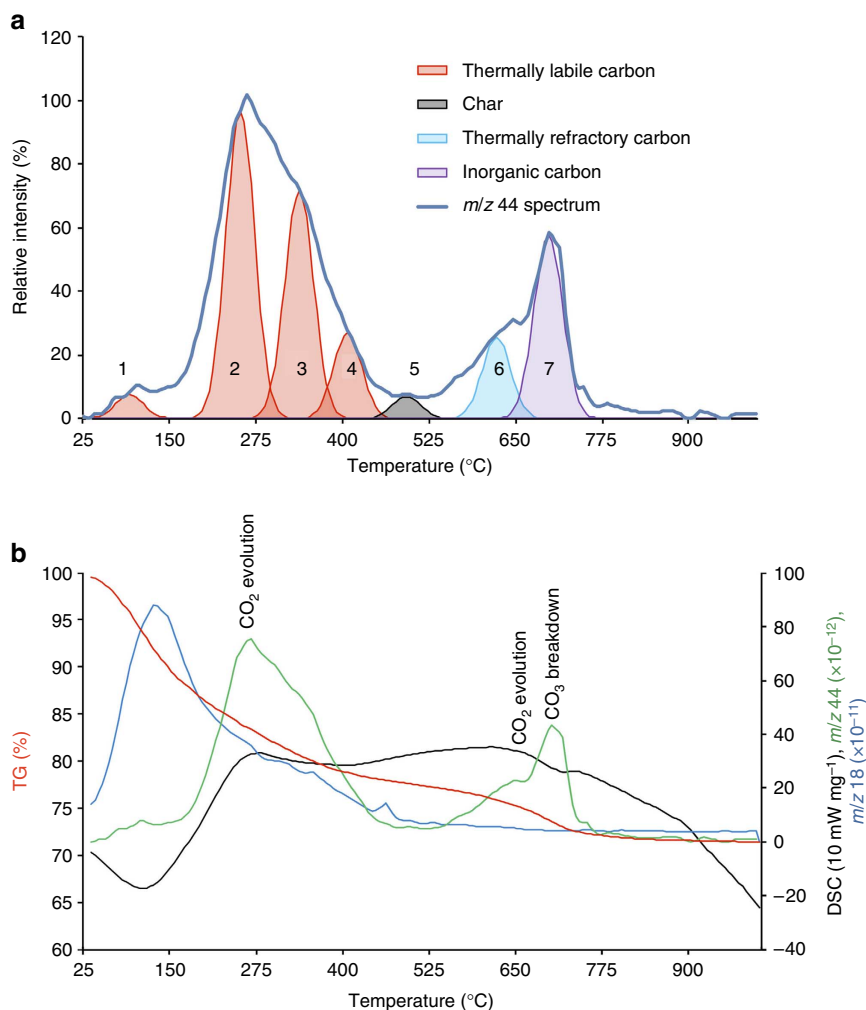


Figure 3 | TGA-DSC data on birnessite coating. (a) Carbon dioxide evolution with temperature and synthesized deconvolution components (see Methods section for more details) for bulk Mn-OC showing thermally labile Mn-OC (in pink), thermally refractory Mn-OC (in blue) and inorganic carbon (in purple; TIC is 0.5%w/wC). (b) Differential scanning calorimetry (black) curve showing labelled CO₂ evolution at 270 and 600 °C (exotherms) and CO₃²⁻ breakdown at 712 °C (endotherm); m/z 44 curve (green); m/z 18 curve (blue) and thermogravimetric weight loss (red).

are therefore confident that the exotherm, which we identify at 600 °C in the bulk birnessite coating, represents material that is inherently present in the coating and not an artefact of burning.

The peak at 600 °C representing thermally refractory OC has not previously been reported in the literature as soil organic matter or mineral-associated organic carbon⁴⁷, but is usually reported as black carbon^{12,13}. The peatlands in the WTW catchment are occasionally burned and so particulate black carbon originating from the peatlands⁴⁴ may be present in the influent water on occasion. However, peat-derived black carbons usually contain detectable N⁴⁸ and the refractory Mn-OC contains no detectable N (see Fig. 4 inset). For this reason it seems more likely that the refractory Mn-OC in our samples is not black carbon but organic matter that is adsorbed to the birnessite and that adsorption to the birnessite surface is the reason why the OC is decomposed more slowly and to a lesser extent than uncomplexed OC³.

To understand the difference in chemical state between the thermally labile and thermally refractory Mn-OC, XPS analysis of the bulk birnessite coating as received (MnOAR Bulk) and the bulk birnessite coating thermally treated to 550 °C (MnO550 Bulk) was undertaken (see Fig. 4). The Mn-OC (available up to 800 °C) in the MnOAR bulk samples contains both 89% thermally labile and 11% thermally refractory Mn-OC;

deconvolution of the XPS data (see Methods section) reveals four components consistent with alkene/aromatic (284.9 eV), aliphatic (286.5 eV), amide (~288 eV, but this peak occurs at the same binding energy as the carboxyl peak component) and carboxyl (288.3 eV) bonds (see Table 2; Fig. 4). In contrast, the thermally refractory Mn-OC (MnO550 Bulk and MnO1000 Bulk, which is the bulk material thermally treated to 550 and 1,000 °C, respectively) contains alkene/aromatic and carbonyl (carbonate and carboxylate) groups only (Table 2; Fig. 4). It should be noted that, in MnO1000 Bulk, the carbonyl compounds are ~60% reduced (*cf.* MnO550 Bulk) and consist of only carboxylate compounds, since the carbonate fraction is decomposed at 712 °C (see Supplementary Fig. 1). This was also confirmed with a high resolution Ca 1s spectra (see Supplementary Fig. 2). The XPS data therefore confirm that the thermally labile and thermally refractory Mn-OC pools are chemically distinct, with the thermally refractory Mn-OC (represented by MnO550) being depleted in N-rich compounds (as shown in the N1s scan inset in Fig. 4).

The bulk birnessite coating as received (MnOAR Bulk) has a C:N ratio of 15:1, which is much lower than the original DOC C:N ratio of 60:1 (ref. 49). This may suggest that selective preservation of N-rich organic material is occurring during the initial adsorption of DOC onto birnessite. A small amount of the

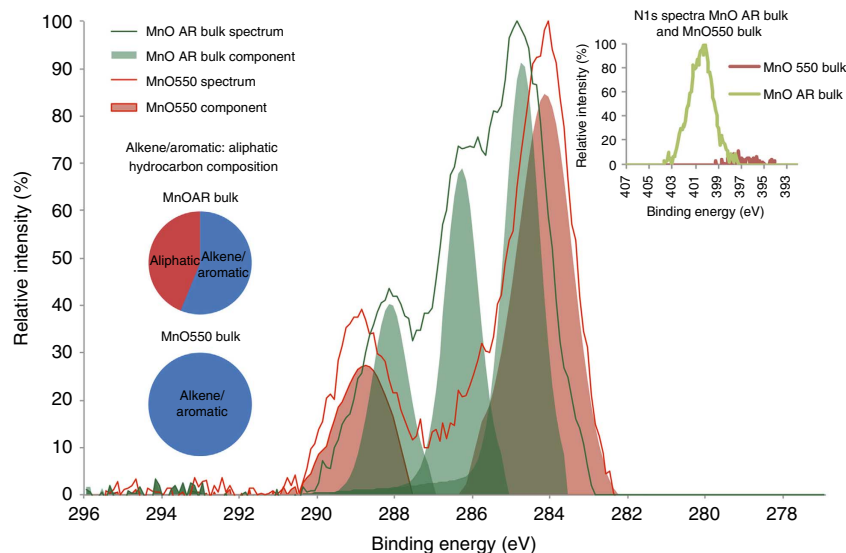


Figure 4 | XPS C1s data on thermally treated bulk birnessite coating. Normalized and mean ($n = 9$) XPS scans of the high-resolution C1s spectra of bulk birnessite coating both as received (MnOAR Bulk) and thermally treated by burning to 550 °C for 8 h (MnO550 Bulk), de-convoluted using synthetic component fitting (see Methods section). There are three main components evident in the bulk birnessite coating, and there are two main components evident in the bulk birnessite coating that has been burned to 550 °C. The most probable chemical assignments for these components are described in Table 2. The pie chart shows the proportion of hydrocarbon that is aromatic or aliphatic in character in each of the 'as received' and 'thermally treated' bulk coating. The inset shows N1s scan. Note 'aromatic' in pie chart actually represents alkene/aromatic peak at ~ 285 eV.

Table 2 | XPS C1s data for birnessite coating.

Component positions (eV)				Chemical state	Principal assignments
MnO AR Surface	MnO AR Bulk	MnO550 Bulk	MnO1000 Bulk*		
285.2	284.9	284.3	284.3	C(=C,-H)	Alkene and aromatic
286.1	286.5	ND	ND	C(-C,-H,-N)	Aliphatic [†]
287.2	Peak hidden [‡]	ND	ND	C(-N,-O)	Amides [‡]
288.6	288.3	288.9	288.9 [§]	C(-O,=O)	Carboxylate and CO ₃ ²⁻

ND, not determined; The mean ($n = 9$) binding energy positions of the synthetic components, fitted to C1s spectra. The potential chemical state assignments for these components for MnOAR Bulk (bulk birnessite coating as received), MnO550 Bulk (bulk birnessite coating thermally treated to 550 °C) and MnO1000 Bulk (bulk birnessite coating thermally treated to 1,000 °C) are based on multiple lines of evidence, obtained from high-resolution C1s (shown above and in Figs 4 and 5 and Supplementary Fig. 1) and N1s (inset in Fig. 4) and Ca 2p scans (see Supplementary Fig. 2), and FTIR spectroscopy (see Fig. 2). The bonding environment in all the samples is more complex than represented here, and the complex chemical environment will contain many overlapping Gaussian components. To simplify the deconvolution analysis, the minimum number of components were fitted to the scans and the component assignment interpretation represents the principal chemical state (see Methods section). The changes in component positions between the MnOAR and thermally treated MnO550 and MnO1000 are primarily the result of the removal of thermally labile organic material during thermal treatment.

*Data not presented in Fig. 4 (see Supplementary Fig. 1)

[†]Thermal treatment to 550 °C that removes N (N1s data presented as inset in Fig. 4) suggests a C-N contribution to this component

[‡]FTIR spectroscopy and N1s high-resolution scan supports amide rather than C-O interpretation

[§]Ca2p high-resolution scans (see Supplementary Fig. 2) and decomposition of carbonate at 712 °C (see Fig. 3) supports a carboxylate rather than a carbonate interpretation.

N in the Mn-OC may be due to selective adsorption of a cationic flocculant used, but this is likely to be a very small component (see Methods). High N concentrations are also present in the Fe-OC of marine sediments⁴. However, this N-rich material is not detectable in the thermally refractory Mn-OC fraction (represented by MnO550 Bulk in Table 2 and inset N1s scan in Fig. 4). As the thermally refractory OC is depleted in N, we argue that it cannot have been formed via the polyphenol-Maillard reaction²³ as this type of polymerization reaction involves condensation between amino acids (which contain N) and polyphenols and/or sugars.

The Mn-OC bound at the surface of the birnessite coatings has a significantly lower ratio of alkene/aromatic:aliphatic hydrocarbons (1:4) compared with the Mn-OC present throughout the bulk birnessite coatings (3:2) (see pie-charts in Fig. 5).

The bulk birnessite coating as received (MnOAR Bulk) has a $\delta^{13}\text{C}$ signature of $\sim -24.9\%$ ($n = 3$, s.d. = 0.1), which is statistically significantly less depleted in $\delta^{13}\text{C}$ compared with

the influent water ($\sim -27.0\%$). Lalonde *et al.*⁴ also found a less depleted $\delta^{13}\text{C}$ signature in Fe-OC in marine sediments, which they attributed to selective sorption of an isotopically less depleted fraction of OC by mineral phases. Interestingly, the bulk birnessite coating that has been thermally treated to 550 °C (MnO550 Bulk, containing only thermally refractory Mn-OC) has a $\delta^{13}\text{C}$ signature of $\sim -27.6\%$ ($n = 3$, s.d. = 0.3) that is statistically significantly different from the bulk material as received ($P < 0.01$) but not statistically significantly different from the influent water signature ($\sim -27.0\%$).

Proposed carbon sequestration and stabilization mechanism.

Our data show for the first time that Mn-OC is adsorbed to the surface of birnessite (and trapped within the mineral) via a strong manganese carboxylate bonds (Fig. 6, point 1). We propose that the DOC molecule is tethered, via carboxylate bonding (Fig. 6, point 1). This allows DOC molecules that contain abundant

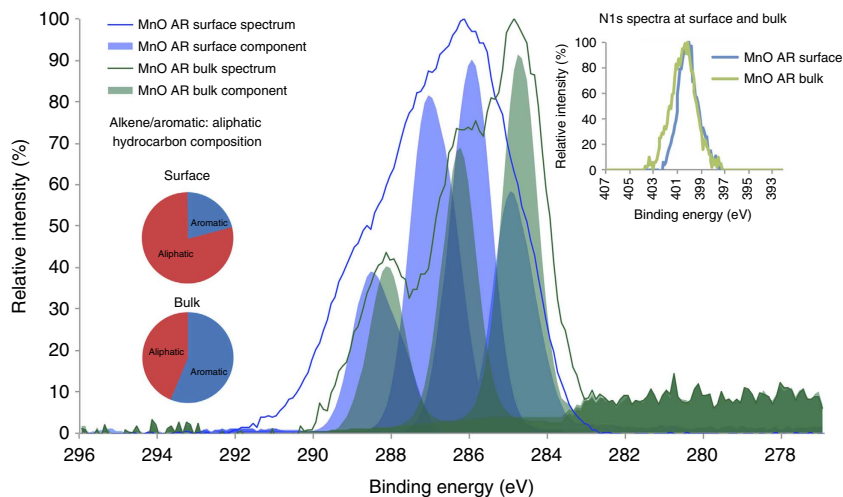


Figure 5 | XPS C1s data comparing surface and bulk birnessite coating. Normalized and mean ($n = 9$) XPS scans of the high resolution C1s spectra of bulk birnessite coating (MnOAR Bulk) and the surface birnessite coating (MnOAR Surface, intact on the sand grain), both as received, de-convoluted using synthetic component fitting (see Methods section). There are three main components evident in the bulk birnessite coating, and there are four main components evident in the surface birnessite coating. The most probable chemical assignments for these components are described in Table 2. The pie chart shows the proportion of hydrocarbon that is aromatic or aliphatic in character in each of the ‘as received bulk’ and ‘as received surface’ coating. Note ‘aromatic’ in pie chart represents alkene/aromatic peak at ~ 285 eV and mean components are not Gaussian. Inset shows N1s scan.

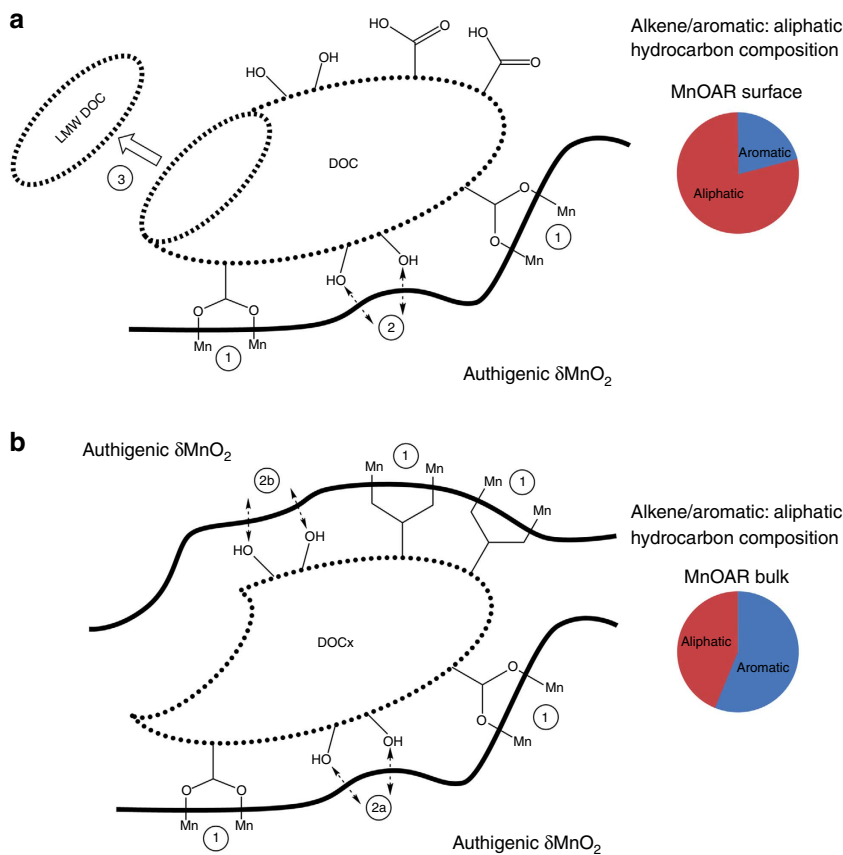
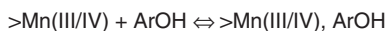
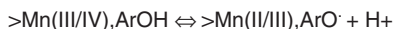


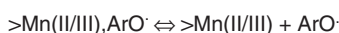
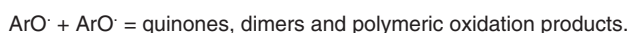
Figure 6 | Hypothesized reaction mechanism between DOC and birnessite. Hypothesized reaction mechanism for conversion of DOC by birnessite coatings both at the surface ((a) points 1-3) and in the bulk material ((b) points 1-2). The dashed arrows represent phenol–birnessite interactions resulting in phenoxy radical formation⁵². The original DOC molecule is oxidized (via the breaking of aromatic bonds⁶) at point 3 resulting in the release of LMW molecules into solution as the birnessite surface is subjected to backwashing in the WTW. The alkene/aromatic:aliphatic ratio (XPS signature) of the resulting smaller molecule DOCx attached to the birnessite surface is shown in pie-chart a. Once DOCx becomes trapped (shown in (b)) the reactions between phenols and the birnessite surface are likely to result in a build up of phenoxy radicals as these are less likely to be washed away at depth in the bulk material. The notably different XPS signature of the bulk material is shown in pie-chart (b).

Precursor complex formation:

Where $>\text{Mn(III/IV)}, \text{ArOH}$ represents either an inner-sphere complex, when the incoming phenols bind directly to surface Mn(III/IV)OH groups, or an outer-sphere complex, in which a layer of coordinated OH^- or H_2O molecules separate phenols from surface groups⁴⁹. It should be noted that inner-sphere reactions are insensitive to the charge of the surface functional groups and incoming ligands⁵⁰.

Electron transfer:

During this step the net flux of Mn(II) and Mn(III) into solution is likely to be negligible⁴⁹, given the fact that the pH of the WTW system is ~ 9 where any released Mn(II) will be effectively re-adsorbed⁴⁹, and Mn(III) oxides have exceedingly low solubility⁵.

Release of phenoxy radical:*Coupling and further oxidation of phenoxy radicals:*

The reaction produces quinones when the concentration of reactants is low. When the concentration of reactants is higher than the reaction produces dimers and polymeric products⁴⁹.

Figure 7 | Reaction scheme between birnessite and phenol groups.

Surface complex formation between birnessite and phenol groups in DOC⁵². In the above reaction scheme the protonation state of the birnessite surface functional groups (as $\text{Mn(III/IV)OH}_2^{2/3}$ or $\text{MnOH(III/IV)}^{-1/3}$), the phenol ion (as ArOH or ArO^-) and reaction intermediates are ignored. However, because the pK_a of poorly crystalline hexagonal birnessite is ~ 2 (ref. 26), while the pK_a of most phenolic $-\text{OH}$ groups is greater than 9 (ref. 52), then at $\text{pH} \sim 9$ in the WTW system, the majority of the birnessite surface groups will be present as negatively charged $\text{Mn(III/IV)OH}^{-1/3}$, while phenol ions will be present as both ArOH or ArO^- .

phenol groups⁵⁰ to react with the birnessite surface (Fig. 6, point 2a). Phenols are known to be a redox mediator⁵¹, capable of catalysing redox reactions, but more importantly they also react with birnessite to form phenoxy radicals via the reactions shown in Fig. 7 (ref. 52).

Phenoxy radicals are then either converted to quinones, or encounters between phenoxy radicals result in radical coupling to produce dimers or polymeric products⁵². Stone⁵² suggests that when the concentration of reactants is low then phenoxy radicals tend to form quinones and that when the concentration of reactants is high, phenoxy radicals will tend to form dimers and polymeric products. Owing to the frequent backwashing in the filter beds it seems likely that the concentration of phenoxy radical containing products at the surface will be kept low as reactants and products are constantly being removed from the surface. We speculate that quinone formation is the most likely reaction pathway occurring between birnessite and DOC molecules at the outermost surface of the birnessite coatings (Fig. 6a). During the course of these reactions, HMW organics are converted to LMW organics (see Fig. 6, point 3) by breaking aromatic bonds⁶, and thus the original DOC molecule is transformed into DOCx, creating the alkene/aromatic: aliphatic ratio of 1:4 that we measure in the surface-bound Mn-OC.

When the next layer of birnessite precipitates, DOCx is then trapped and the uppermost surface of the DOCx molecule can adsorb to the new birnessite surface via the manganese carboxylate bonds (also labelled point 1 in Fig. 6), instigating further phenolic–birnessite interactions (labelled as point 2b on Fig. 6b). If the redox reactions between phenol groups and birnessite occurring at depth within the bulk material were the same as at the surface then the ratio of alkene/aromatic: aliphatic ratio should theoretically continue to decrease, as more redox reactions occur breaking up more aromatic bonds. However, the ratio of alkene/aromatic:aliphatic actually increases significantly from 1:4 in surface-bound Mn-OC to 3:2 in the bulk Mn-OC. We do not know the reason for this stark change in carbon chemistry. The main difference in the reaction environment is that at the surface of the birnessite any reaction products formed could be removed by backwashing, whereas in the bulk material, which is not exposed to backwashing, phenol–birnessite interactions are more likely to lead to a build-up of phenoxy radical containing products that could lead to dimer formation and polymeric products⁵². However, the mechanisms presented in Fig. 7 are likely to occur as a continuum between surface and at depth within the bulk material.

Polymerization of phenoxy radicals can create C-C bonds and C-O bonds linking benzene rings⁵³. These bonds are aliphatic suggesting polymerization should result in an XPS signature with a lower alkene/aromatic: aliphatic ratio. However, our XPS data show a significant increase in the alkene/aromatic: aliphatic ratio. There has been much work carried out on the cross-coupling of phenolic molecules with humic substances using NMR⁵⁵ but no published literature as far as the authors are aware on the XPS signature of such linkages. It is possible that C-C bonds that link benzene rings could lead to an increased alkene/aromatic signal due to the more polymerized nature of the products but we have no evidence for this. The XPS data do not contradict the formation of C-O (ester or ether bonds) either, but, because the carbonyl bond occur at binding energies that overlap with ether bonds, XPS cannot discriminate between the C-O bonds. We are not suggesting that the thermally refractory nature of the Mn-OC is due to polymerization, we only invoke this reaction pathway to explain the stark change in alkene/aromatic:aliphatic ratio between surface-bound Mn-OC and bulk Mn-OC.

We observe with TEM 7 and 10 Å birnessite in the Mn oxide coating (see Fig. 1). We know that 10 Å birnessite can form from 7 Å birnessite as a secondary precipitate during dissolution–recrystallisation reactions under diagenesis⁵⁴. We also know that physical entrapment of C can also cause 10 Å birnessite to form from 7 Å birnessite⁵⁵. The presence of 10 Å birnessite in our system is therefore consistent with the diagenetically driven redox reactions and physical entrapment of OC that we postulate.

Discussion

Clearly the WTW presents environmental conditions different from most natural terrestrial and marine environments. Indeed it is precisely this controlled environment that has allowed us to gain a fundamental understanding of the underlying reaction mechanisms that are responsible for the sequestration and stabilization of organic carbon by birnessite. To evaluate what role natural birnessites play in sequestering and transforming carbon on a global scale, however, more research is required, specifically to determine whether the components of the WTW system are similar enough to natural environments to provide a representative analogue.

While we identify poorly crystalline hexagonal birnessite in the WTW, which is one of the most common Mn oxide minerals present in terrestrial^{18,19} and marine systems^{20–22}, there are

potentially important differences between the WTW birnessite and that found in natural environments. This could hint to additional reaction mechanisms, and affect the reaction rate, of organic carbon sequestration and transformation. For example, differences in the pH at which birnessite is precipitated (where the WTW birnessite is precipitating at a higher pH (pH 9) than in most natural environments (rivers typically being ~pH 6–8 and seawater ~pH 8)) and/or the influence of Mn(II) oxidation by microorganisms (where the WTW birnessite is likely precipitated via the abiotic oxidation of Mn(II/III), while it is known that microorganisms can significantly enhance Mn oxidation in natural systems⁵⁶) can result in subtle structural differences between different poorly crystalline hexagonal birnessites⁵⁷, which could influence the rate at which organic carbon is sequestered and stabilized.

Importantly, having a controlled system has allowed us to identify a fundamental mechanism for how birnessite can trap and stabilize organic carbon. Specifically, we have determined that carboxylate groups are involved in bridging and/or bidentate bonds that bind DOC molecules to birnessite, both at the mineral surface and within the bulk mineral, and that these bonds at least partly withstand washing with 1 M NaOH solution. We conclude that this bonding of DOC by carboxylate groups, in conjunction with the physical trapping of DOC within the ‘onion shell’ layers of the birnessite coating, is responsible for the thermally refractory nature of 11% of the Mn-OC (that is Mn-OC which is available to 800 °C). Further research is required to confirm whether OC is physically trapped in birnessite found in the natural environment.

Furthermore, we propose that phenol groups within the DOC molecule are oxidatively transformed to phenoxy radicals, following the well-known birnessite-phenol reaction pathway⁵², leading to a continuum of reactions from surface to bulk material, including the production of LMW organic molecules (with potential complete mineralization to CO₂ and H₂O) and the formation of polymerized products in the bulk material where the concentration of phenoxy radical products can build up⁵². Whether birnessite can catalyse the polymerization of sequestered organic carbon, and how this process might affect the fate of buried organic carbon in natural systems is not known and requires further research. However, as birnessite is effectively recycled at oxic-anoxic redox interfaces⁵⁸, the strong association between Mn and C may not be preserved in the deeper geological record⁸. It is therefore important to note that only a spectrum of studies looking at both controlled and natural systems will allow us to fully understand the relation between OC and metal (hydr)oxides.

We suggest that this initial mechanistic understanding of the role of birnessite in carbon stabilization may help in our understanding of the global carbon cycle.

Methods

Water treatment works. The birnessite-coated sands come from Mosswood Water Treatment Works (WTW) in the UK (54°51′N–53°59′W). Mosswood is a Mn-removing WTW (owned by Northumbrian Water Ltd, UK) that employs chemical oxidation and filtration to remove dissolved Mn(II) from potable water. Such WTWs are prevalent globally in temperate regions where influent water contains dissolved Mn and DOC, which are both problematic for the water industry for aesthetic reasons⁵⁹. Soluble Mn(II) undergoes sorption to filter sand surfaces followed by oxidation to insoluble manganese oxides utilizing the autocatalytic nature of manganese oxidation at pH9. Some anthracite is also used as an additional filter media. ¹⁴C analysis was used to confirm that the bulk Mn-OC is 100% modern organic matter to ensure that there was no interference from the anthracite.

Northumbrian Water Ltd. confirmed that these sands were in place for ~40 years. Replacement of the filter media usually takes place due to drop in Mn removal efficiency either due to lack of porosity or an unknown cause. The influent water at Mosswood (132.5 Ml per day) originates from the Pennines peat uplands and influent water TOC is ~10 mg l⁻¹ present as both particulate organic carbon (POC or suspended solids) and dissolved organic carbon (DOC). Dissolved Mn is

~0.2 mg l⁻¹. Ferric sulphate is added as a coagulant to the influent water at the WTW to remove the majority of suspended solids (both organic and inorganic particulates) in the secondary treatment process before the water enters the Mn filter beds. A flocculant (a modified starch with cationic amine groups) is also added at very low dosage rates (*cf* natural DOC which is > 1,000 kg day⁻¹) in the secondary treatment process and most of this is removed as flocculated solids known as water treatment residual. Any flocculant remaining in solution could enter the Mn filter beds but the ratio of influent DOC to flocculant is likely to be high and we assume that the flocculant does not constitute a large part of the Mn-OC.

The birnessite-coated sand was analysed in two fractions, at the surface of the intact coating and at depth that was represented by the bulk material separated from the sand grain. The 63–149 μm fraction of the birnessite coating (captured from sieved intact sand grains by shaking) was (arbitrarily) used to represent the bulk material. All the other size fractions also contained ~3%w/wC. TC, TIC, TOC and N were determined using a LECO Elemental analyser. Organic carbon (carbonate-free) isotopic abundances were analysed by IsoAnalytical Ltd (Crewe, UK), using a Europa Scientific 20:20 instrument (up to 1,700 °C). Results were recorded relative to the Vienna Pee Dee Belemnite standard (v-PDB). Samples were acid washed with 2 M hydrochloric acid and analysed by elemental analyser-isotope ratio mass spectrometry. Replication had a s.d. better than ± 0.1‰ and values for reference materials were within two s.d. of the expected result. ¹⁴C analysis was carried out at SUERC (Glasgow University) to confirm that Mn-OC was not anthracite.

Thermogravimetric analysis. Thermal analysis was carried out to determine the relative proportions of different C components according to the method of Lopez-Capel *et al.*⁴³, extended by determination of evolved gases. A Netzsch STA 449C Jupiter TG-DSC system connected by a heated capillary (200 °C) to a Netzsch Aeolos quadrupole mass spectrometer system was used to determine the following parameters: (1) mass change, (2) energy gained or lost from the sample, (3) composition of evolved gases (*m/z* range 10–300). Individual powder samples (typically 10 mg) were placed within an alumina crucible, using an identical empty reference crucible, and were heated from ambient temperature to 990 °C under flowing He80-O20. Intensities for *m/z* 44 (CO₂ + N₂O) and *m/z* 18 (H₂O) were recorded. No correction was made to *m/z* 44 for evolved N₂O, which was assumed to be negligible compared with CO₂ given failure to detect measurable *m/z* 30 (NO). Evolved gas evolution curves were interpreted using GRAMS/AI peak fitting software (www.AdeptScience.co.uk) that permits investigation of the contribution of several individual peaks to an overall trace. By defining initial conditions (including a presumed Gaussian peak shape), the range of potential values for each peak centre (25–200 °C, 200–375 °C, 375–550 °C and 550–800 °C respectively) and the number of iterations to perform (in this case 50), the software fits individual labile, recalcitrant and refractory carbon peaks⁶⁰ such that their combined shapes and areas are the best possible fit for the overall CO₂ trace.

Thermal treatment (to generate MnO500 and MnO1000 samples) was conducted by placing 2 g sample in a ceramic thimble then heated for 8 h in a 6 litre Carbolite ELF muffle furnace and allowed to cool to ambient temperature before being placed in 10 ml glass vials and sealed with Al foil between the screw caps for storage.

Focused ion beam, scanning electron and transmission microscopy. FIB cross-sections were performed using FEI Helios Nano Lab 600 Dual Beam system, equipped with focused Ga liquid metal ion source. Ion beam thinning carried out at 52° with respect to electron column. Initially a ‘rough cut’ was carried out after depositing a protective platinum layer *in situ* using a gas injection system. Several *in situ* polishing steps were performed on exposed cross-sections to produce a clean surface with minimal beam damage. High-resolution backscattered electron imaging was carried out in the same system, with images being captured using a low kV immersion lens.

SEM imaging was performed on a Hitachi SU70 high-resolution analytical SEM, equipped with Oxford instruments INCA energy 450 and WDS 700. The JEOL 2100F transmission electron microscope was operated at 80 KeV.

Micro-FTIR analyses were carried out using a Perkin Elmer Spotlight FT-IR imaging system. Reflectance micro Fourier Transmitted Infrared spectra were collected over the 4,000 to 700 cm⁻¹ wavenumber range, at a resolution of 4 cm⁻¹, beam diameter 15 μm.

X-Ray photoelectron spectroscopy. XPS spectra were obtained at the National EPSRC XPS Users’ Service (NEXUS) at Newcastle University. 0.5 grams of sample was immobilized onto a Si wafer using 3M double-sided adhesive. The immobilized samples were decontaminated within the instrument by sputter etching, using a Ag⁺ gas cluster ion beam (GCIB) gun at 4 kv for 30 s. The Ag⁺ GCIB sputter etching was carried out in polyatomic mode to avoid degrading the chemistry during the etching process. The samples were then analysed using a Thermo-scientific K-alpha X-ray photoelectron spectrometer (XPS) (Thermo-scientific, East Grinstead, UK).

Low-resolution full spectra were acquired using a monochromatic Al Kα X-ray source with an output energy of 1,486.6 eV. An X-ray beam spot size of 50 μm, and a dwell time of 100 ms was used for both high resolution and survey spectra. The surface charge compensation was achieved using a low-energy electron flood gun,

which was operated at 40 eV. Survey spectra were obtained between a binding energy of 0 and 1,350 eV with a 1.0 eV step size and pass energy of 200 eV.

Analysis of the survey spectra was carried out using CasaXPS software (Teighmouth, UK), and major peaks were selected for element identification using the Handbook of X-ray Photoelectron Spectroscopy⁶¹. The major peaks for carbon and nitrogen were selected for high-resolution scans from the survey spectra. C1s high-resolution spectra were obtained from binding energies of 279.0 to 298.0 eV and N1s high-resolution spectra between 410.0 and 392.0 eV. The step size for the high-resolution spectra was 0.1 eV with a 40 eV pass energy. Shirley backgrounds were applied to the high-resolution spectra and the minimum number of synthetic Gaussian components were fitted to the C1s high-resolution scans to elucidate the chemical states of the carbon using the CasaXPS software algorithm. The NIST (srdata.nist.gov/xps) and LA surface (lasurface.com) databases were used for component peak assignment in conjunction with other references^{61,62}.

The spectral data of the peaks, their components and their backgrounds, from each of the replicates, were acquired from the C1s and the N1s high-resolution scans. These were obtained from the surface fraction, the bulk fraction and the 550 and 1,000 °C thermally treated samples. The digital CasaXPS spectral data were transferred to Microsoft Excel 2010. The mean spectral intensity of replicates and their components were calculated and the mean Shirley backgrounds were deducted. The mean data were then normalized to the highest spectral intensity. The mean normalized spectra and their normalized mean components were then plotted against binding energy.

Data availability. The data presented in this paper are available from <http://dx.doi.org/10.15128/br86b364d>.

References

- Hedges, J. I. & Keil, R. G. Sedimentary organic-matter preservation—An assessment and speculative synthesis. *Mar. Chem.* **49**, 81–115 (1995).
- Keil, R. G. & Mayer, L. M. Mineral matrices and organic matter. *Treatise on Geochemistry*. 2nd edn 337–359 (2014).
- Kaiser, K. & Guggenberger, G. Mineral surfaces and soil organic matter. *Eur. J. Soil Sci.* **54**, 219–236 (2003).
- Lalonde, K., Mucci, A., Ouellet, A. & Gelinas, Y. Preservation of organic matter in sediments promoted by iron. *Nature* **483**, 198–200 (2012).
- Stone, A. T. & Morgan, J. J. Reduction and dissolution of manganese (III) and manganese (IV) oxides by organics. 2. Survey of the reactivity of organics. *ES&T* **18**, 617–624 (1984).
- Sunda, W. G. & Keiber, D. J. Oxidation of humic substances by manganese oxides yields low molecular weight substrates. *Nature* **367**, 62–64 (1994).
- Lovley, D. Dissimilatory Fe(III) and Mn(IV) reduction. *Microb. Rev.* **55**, 259–287 (1991).
- Roy, M. *et al.* Reactive iron and manganese distributions in seabed sediments near small mountainous rivers off Oregon and California (USA). *Continental Shelf Res.* **54**, 67–67 (2013).
- Hedges, J. I. *et al.* The molecularly-uncharacterised component of nonliving organic matter in natural environments. *Org. Geochem.* **31**, 945–948 (2000).
- Schmidt, M. W. I. *et al.* Persistence of soil organic matter as an ecosystem property. *Nature* **478**, 49–56 (2011).
- Hammes, K. *et al.* Comparison of quantification methods to measure fire-derived (black/elemental) carbon in soils and sediments using reference materials from soil, water, sediment and the atmosphere. *Global Biogeochem. Cycles* **21**, GB3016 (2007).
- De la Rosa, J. M., Lopez Capel, E., Gonzalez-Vila, F. J., Gonzalez-Perez, J. A. & Manning, D. A. C. Direct detection of black carbon in soils by Py-GC/MS, 13C NMR spectroscopy and thermo gravimetric techniques. *Am. J. Soil Sci. Soc.* **72**, 258–267 (2008).
- De la Rosa, J. M. *et al.* Structural properties of non-combustion derived refractory organic matter which interfere with BC quantification. *J. Anal. Appl. Pyrolysis* **85**, 299–308 (2009).
- Vandenbroucke, M. & Largeau, C. Kerogen origin, evolution and structure. *Org. Geochem.* **38**, 719–833 (2007).
- Burdige, D. J. Preservation of organic matter in marine sediments: Controls, mechanisms, and an imbalance in sediment organic carbon budgets? *Chem. Rev.* **107**, 467–485 (2007).
- von Lutzow, M. *et al.* Stabilization of organic matter in temperate soils: mechanism and their relevance under different soil conditions: a review. *Eur. J. Soil Sci.* **57**, 426–445 (2006).
- Collins, M. J., Bishop, A. N. & Farrimond, P. Sorption by mineral surfaces—rebirth of the classical condensation pathway for kerogen formation. *GCA* **59**, 2387–2391 (1995).
- McKenzie, R. M. Manganese oxides and hydroxides. In: *Minerals in Soil Environments*. Eds. Dixon, J. B. & Weed, S. B. Soil Sci. Soc. Am., 1988).
- Elzinga, E. J. Reductive transformation of birnessite by aqueous Mn(II). *ES&T* **45**, 6366–6372 (2011).
- Burns, R. G. & Burns, V. M. Mineralogy and crystal-chemistry of deep-sea manganese nodules, a polymetallic resource of the 21st century. *Phil. Trans. R. Soc. A—Maths. Phys. Eng. Sci.* **286**, 283–301 (1977).
- Post, J. E. Manganese oxide minerals: Crystal structures and economic significance. *Proc. Natl Acad. Sci. USA* **96**, 3447–3454 (1999).
- Cronan, D. S. & Tooms, J. S. The geochemistry of manganese nodules and associated pelagic deposits. *Deep Sea Res.* **16**, 335–359 (1969).
- Jokic, A., Wang, M. C., Frenkel, A. I. & Huang, P. M. Integration of the polyphenol and Maillard reactions into a unified abiotic pathway: the role of δ -MnO₂. *Org. Geochem.* **35**, 747–762 (2004).
- ChangChien, S. W., Chen, H. L., Wang, K. & Seshiah, K. Oxidative degradation and associated mineralization of catechol, hydroquinone and resorcinol catalyzed by birnessite. *Chemosphere* **74**, 1125–1133 (2009).
- Tipping, E., Billett, M. F., Bryant, C. L., Buckingham, S. & Thacker, S. A. Sources and ages of dissolved organic matter in peatland streams: evidence from chemistry, mixture modeling and radiocarbon data. *Biogeochemistry* **100**, 121–137 (2010).
- Chorover, J. & Amistadi, M. K. Reaction of forest floor organic matter at goethite, birnessite and smectite surfaces. *GCA* **65**, 95–109 (2001).
- Stevenson, F. J. *Humus Chemistry: Genesis, Composition, Reactions* (Wiley, 1994).
- Mitchell, G. D., Davis, A. & Chander, S. Surface properties of photo-oxidized bituminous vitrains. *Int. J. Coal Geol.* **62**, 33–47 (2005).
- Skoog, D. A. & Leary, J. J. *Principles of Instrumental Analysis* (Saunders College, 1992).
- Wade, L. G. *Organic Chemistry* (Prentice-Hall, 1995).
- Deacon, G. B. & Phillips, R. J. Relationships between the carbon-oxygen stretching frequencies of carboxylate complexes and the type of carboxylate coordination. *Coord. Chem. Rev.* **33**, 227–250 (1980).
- Tackett, J. E. FT-IR characterisation of metal acetates in aqueous-solution. *Appl. Spectrosc.* **43**, 483–489 (1989).
- Nakamoto, K. *Infrared and Raman Spectra of Inorganic and Coordination Compounds*. Part B5th edn (John Wiley & Sons, 1997).
- Chu, H. A., Hillier, W. & Debus, R. J. Evidence that the C-terminus of the D1 polypeptide of photosystem II is ligated to the manganese ion that undergoes oxidation during the S-1 to S-2 transition: An isotope-edited FTIR study. *Biochemistry* **43**, 3152–3166 (2004).
- Ojeda, J. J., Romero-Gonzalez, M. E., Pouran, H. M. & Banwart, S. A. In-situ monitoring of the biofilm formation of *Pseudomonas putida* on hematite using flow-cell ATR-FTIR spectroscopy to investigate the formation of inner-sphere bonds between the bacteria and the mineral. *Mineral. Mag.* **72**, 101–106 (2008).
- Durand, J. P., Senanayake, S. D., Suib, S. L. & Mullins, D. R. Reaction of formic acid over amorphous manganese oxide catalytic systems: an in situ study. *J. Phys. Chem. C* **114**, 20000–20006 (2010).
- Conley, R. T. *Infrared Spectroscopy* (Allyn and Bacon, 1972).
- Philipp, R. & Fujimoto, K. FTIR study of CO₂ Adsorption/desorption on MgO/CaO catalysts. *J. Phys. Chem.* **96**, 9035–9038 (1992).
- Her, N., Amy, G., McKnight, D., Sohn, J. & Yoon, Y. Characterisation of DOM as a function of molecular weight by fluorescence EEM and HPLC-SEC using UVA, DOC and fluorescence detection. *Water Res.* **37**, 4295–4303 (2003).
- Gonzalez, C. *et al.* Transformations of manganese oxides under different thermal conditions. *J. Thermal. Anal.* **47**, 93–102 (1996).
- Morgan, D. J., Milodowski, A. E., Warne, S. St. J. & Warrington, S. B. Atmospheric dependence of the thermal decomposition of manganite, γ -Mn-OH. *Thermochim. Acta* **135**, 273–277 (1988).
- Lopez-Capel, E., Sohi, S. P., Gaunt, J. L. & Manning, D. A. C. Use of thermogravimetry-differential scanning calorimetry modelable soil organic matter fractions. *Soil Sci. Soc. Am. J.* **69**, 136–140 (2005).
- Lopez-Capel, E., Abbott, G. D., Thomas, K. M. & Manning, D. A. C. Coupling of thermal analysis with quadrupole mass spectrometry and isotope ratio mass spectrometry for simultaneous determination of evolved gases and their carbon isotopic composition. *J. Anal. Appl. Pyroly.* **75**, 82–89 (2006).
- Golden, D. C., Dixon, J. B. & Chen, C. C. Ion exchange, thermal transformations and oxidizing properties of birnessite. *Clays Clay Miner.* **34**, 511–520 (1986).
- Landon, B., Drits, V. A., Qi, Feng & Mancaeu, A. Structure of synthetic Na-birnessite: evidence for a triclinic one-layer unit cell. *Am. Mineral.* **87**, 1662–1671 (2002).
- Leifeld, J. Thermal stability of black carbon characterised by oxidative differential scanning calorimetry. *Org. Geochem.* **38**, 112–127 (2007).
- Plante, A., Fernandez, J. M. & Leifeld, J. Application of thermal analysis techniques in soil science. *Geoderma* **153**, 1–10 (2009).
- Almendros, G., Knicker, H. & Gonzalez-Vila, F. J. Rearrangement of carbon and nitrogen forms in peat after progressive thermal oxidation as determined by solid-state ¹³C- and ¹⁵N-NMR spectroscopy. *Org. Geochem.* **34**, 1559–1568 (2003).
- Worrall, F., Clay, G. D., Burt, T. D. & Rose, R. The multi-annual nitrogen budget of a peat-covered catchment—changing from sink to source? *Sci. Total Environ.* **433**, 178–188 (2012).
- Thorn, K., Arterburn, J. & Mikita, M. ¹⁵N and ¹³C NMR investigation of hydroxylamine-derivatised humic substances. *ES&T* **26**, 107–116 (1992).

51. Van der Zee, F. R. & Cervantes, F. J. Impact and application of electron shuttles on the redox (bio)transformation of contaminants: A review. *Biotechnol. Adv.* **27**, 256–277 (2009).
52. Stone, A. T. Reductive dissolution of Mn (III/IV) oxides by substituted phenols. *ES&T* **21**, 979–988 (1987).
53. Hatcher, P. G., Bortlatynski, J. M., Minard, R. D., Dec, J. & Bollag, J. M. Use of high-resolution ^{13}C NMR to examine the enzymatic covalent binding of ^{13}C labelled 2,4-dichlorophenol to humic substances. *ES&T* **27**, 2098–2103 (2003).
54. Bodei, S., Manceau, A., Geoffroy, N., Baronnet, A. & Buatier, M. Formation of todorokite from vernadite in Ni-rich hemipelagic sediments. *GCA* **71**, 5698–5716 (2007).
55. Jiang, W.-T. *et al.* Removal of ciprofloxacin from water by birnessite. *JHM* **250-251**, 362–369 (2013).
56. Tebo, B. M. *et al.* 'Biogenic manganese oxides: Properties and mechanisms of formation'. *Annu Rev Earth Planet. Sci.* **32**, 287–328 (2004).
57. Webb, S. M., Tebo, B. M. & Bargar, J. R. Structural influences of Na and Ca ions on the biogenic Mn oxides produced by the marine *Bacillus* Sp., Strain SG-1. *Geomicrobiol. J.* **22**, 181–193 (2005).
58. März, C. *et al.* Manganese-rich brown layers in Arctic Ocean sediments: composition, formation mechanisms and diagenetic overprint. *GCA* **75**, 7668–7687 (2011).
59. Hu, P. -Y., Hsieh, Y. -H., Chen, J. -C. & Chang, C. -Y. Adsorption of divalent manganese ion on manganese-coated sand. *J. Water Supply: Res. Technol.* **53**, 151–158 (2004).
60. Manning, D. A. C., Renforth, P., Lopez-Capel, E. & Robertson, S. A. Carbonate precipitation in artificial soils produced from 'wastes': an opportunity for passive carbon sequestration. *Int. J. Greenhouse Gas Control* **17**, 309–317 (2013).
61. Chastain, J. & King, R. C. (eds) *Handbook of X-ray photoelectron spectroscopy: a reference book of standard spectra for identification and interpretation of XPS data* (Physical Electronics Division, Perkin-Elmer Corporation, 1995).
62. Beamson, G. & Briggs, D. *High resolution XPS of organic polymers: the Scienta ESCA300 database 4* (Wiley, 1992).

Acknowledgements

This research was financially supported by grants from the UK Engineering and Physical Sciences Research Council (EP/G028958/1) and Leverhulme Trust (Engineering Prize, 2011). The data presented in this paper are available from <http://dx.doi.org/10.15128/br86b364d>.

We thank the staff at Northumbrian Water for their support of this research. We thank Ed Tipping (Lancaster University), Andy Beeby, Darren Grocke and David Apperley (Durham University), Clare McCann, Geoff Abbott, Maggie White, Naoko Sano and Peter Cumpton, (Newcastle University), Andy Baker (University of New South Wales), Brad Tebo (Oregon Health and Science University), Alan Stone and Ted Goldstein (John Hopkins University), Karen Hudson-Edward (Birkbeck) and Charlotte Bryant (NERC) for their constructive advice throughout the research. Thanks also to Christine Jeans (Newcastle University) for all her work on the graphics.

Author contributions

K.J. conceived and led the project, G.P. carried out XPS, and E. L.-C. carried out TGA. C.P. provided mineralogical expertise and together with N.G. and C.M. helped develop the mechanistic understanding. T.W. helped shape the wider implications of the work. N.F. and S.R. carried out wet chemistry experiments and collected fluorescence spectroscopic data. L.B. produced the SEM, TEM and FIB images, J.O. provided expertise in IR spectroscopy, and F.W. and C.G. advised on TGA analysis and stable isotopes respectively. All authors contributed to writing the paper.

Additional information

Supplementary Information accompanies this paper at <http://www.nature.com/naturecommunications>

Competing financial interests: The authors declare no competing financial interests.

Reprints and permission information is available online at <http://npg.nature.com/reprintsandpermissions/>

How to cite this article: Johnson, K. *et al.* Towards a mechanistic understanding of carbon stabilization in manganese oxides. *Nat. Commun.* **6**:7628 doi: 10.1038/ncomms8628 (2015).



This work is licensed under a Creative Commons Attribution 4.0 International License. The images or other third party material in this article are included in the article's Creative Commons license, unless indicated otherwise in the credit line; if the material is not included under the Creative Commons license, users will need to obtain permission from the license holder to reproduce the material. To view a copy of this license, visit <http://creativecommons.org/licenses/by/4.0/>